Asian Journal of Chemistry; Vol. 38, No. 2 (2026), 403-410
ASIAN JOURNAL OF CHEMISTRY
https://doi.org/10.14233/ajchem.2026.35011

# Effect of Crystallinity and Optical Tuning in Sonochemically Synthesised ZnO Nanoparticles for Enhanced Photocatalytic Efficiency

VIKAS G. PATIL[1,2,*], MADHAV MANE[3], SANTOSH B. KATARIYA[3] and D.V. MANE[4]

[1]School of Sciences, Yashwantrao Chavan Maharashtra Open University, Nashik-420003, India
[2]Department of Sciences, K.J. Somaiya Polytechnic, Mumbai-400077, India
[3]Department of Chemistry, SIES College of Arts, Science and Commerce, (Autonomous) Sion, Mumbai-400022, India
[4]Department of Chemistry, Shri Chhatrapati Shivaji College Omerga, Dharashiv-413606, India

*Corresponding author: E-mail: vikasgpatil8@gmail.com

*Received*: 5 October 2025 *Accepted*: 30 December 2025 *Published online*: 31 January 2026 AJC-22257

In this work, phase-pure ZnO nanoparticles were synthesized *via* an ultrasonic-assisted sonochemical route and systematically characterized to elucidate their structural, thermal, optical, and photocatalytic properties. Thermogravimetric analysis revealed a minor mass loss (~3.5%) below 400 ºC, attributed to the removal of surface-adsorbed organic species, confirming the subsequent thermal stability of ZnO NPs. X-ray diffraction analysis confirmed the formation of a single-phase hexagonal wurtzite structure (space group $P6_3mc$) with a lattice parameter a = 3.517 Å and an average crystallite size of 21.6 nm, as estimated by the Debye-Scherrer equation. Energy-dispersive X-ray spectroscopy verified the stoichiometric Zn:O composition, with trace carbon arising from residual surface species. Scanning and transmission electron microscopy revealed quasi-spherical polycrystalline aggregates with a mean particle size of 48.22 nm. High-resolution TEM analysis displayed well-defined lattice fringes with interplanar spacings of 0.28 nm (100) and 0.26 nm (002), indicating the presence of single-crystalline domains within the aggregates. FT-IR spectroscopy confirmed residual organic functional groups alongside characteristic Zn–O vibrational modes in the 848-404 $cm^{-1}$ range. UV-visible spectroscopy demonstrated a widened direct bandgap of 3.27 eV, indicative of quantum confinement effects. Photocatalytic performance evaluated under 366 nm UV irradiation showed efficient degradation of methylene blue (10 ppm), achieving over 50% removal within 160 min and following pseudo-first-order kinetics. The combined effects of high crystallinity, bandgap modulation and surface reactivity underscore the potential of these ZnO nanoparticles as effective photocatalysts for advanced oxidation processes in environmental remediation.

**Keywords: ZnO nanoparticles, Sonochemical method, Methylene blue dye, Photocatalytic activity.**

## INTRODUCTION

Zinc oxide nanoparticles (ZnO NPs) have attracted sustained attention in materials science owing to their exceptional and tunable physico-chemical properties, which enable broad functionality across environmental, electronic and energy related applications [1]. This intrinsic crystallographic asymmetry underpins its attractive optoelectronic, piezoelectric and pyroelectric properties [2]. Notably, the crystallinity and defect landscape of ZnO play a decisive role in governing charge transport, light-matter interactions and catalytic performance [3].

At the nanoscale, ZnO exhibits a highly tailorable electronic structure, wherein crystallite size, lattice strain, surface states and oxygen vacancy concentration collectively influence the optical absorption and charge-carrier dynamics [4]. The controlled modulation of these parameters is critical for enhancing photocatalytic efficiency, as high crystallinity minimizes bulk recombination while surface defects facilitate charge separation and redox reactions [5]. Consequently, synthesis strategies that enable precise control over crystallinity and optical properties are of dominant importance [6].

Sonochemical synthesis has emerged as a versatile and efficient solution-phase approach for producing ZnO NPs with tunable structural and electronic characteristics [7]. The method relies on acoustic cavitation, where the collapse of transient microbubbles generates localized extreme conditions of temperature and pressure, driving rapid nucleation and non-equilibrium crystal growth [8]. Key reaction parameters like ultrasonic frequency and power density, irradiation time,

precursor concentration, solution temperature and the use of growth-directing agents such as polyvinylpyrrolidone (PVP) or surfactants like sodium dodecyl sulfate (SDS) also govern particle size, crystallinity, defect density and agglomeration behaviour [9]. The dynamic reaction environment promotes the formation of diverse ZnO nanostructures (*e.g.* nanospheres, nanorods and hierarchical assemblies) with high crystallinity and tunable oxygen vacancy concentrations [10,11]. Enhanced crystallinity improves charge mobility, while controlled band-gap widening or narrowing through size and defect engineering directly influences light absorption and photocatalytic kinetics [12].

Beyond photocatalysis, the strong piezoelectric response of ZnO enables piezocatalytic activity under mechanical or ultrasonic stimulation, expanding its utility in wastewater treatment and piezotronic devices [13]. Its wide direct bandgap and high exciton binding energy further support applications in UV photodetectors [14], light-emitting diodes [15] and transparent conducting oxides [16]. In ultrasmall ZnO NPs (< 10 nm), quantum confinement effects induce size-dependent optical transitions, yielding tunable photoluminescence suitable for bioimaging, optical sensing and diagnostics [17-19]. Moreover, applications include mechanical energy harvesting nanogenerators [20], strain sensors [21], antibacterial agents [22], gas sensors [23], UV-blocking additives in sunscreens and protective coatings [24] and nucleating agents in polymer composites [25].

Compared with conventional wet-chemical routes, sonochemical synthesis offers distinct advantages including ambient pressure operation, accelerated reaction kinetics, improved energy efficiency and scalability. However, prolonged high-intensity ultrasonication may lead to probe tip erosion, potentially introducing trace metallic contaminants, which necessitates careful optimization of synthesis conditions [26]. Hence, based on strong inter-dependence between crystallinity, optical tuning and photocatalytic performance, this study focuses on the sonochemical synthesis of ZnO NPs with controlled structural and electronic properties, aiming to elucidate their role in enhancing photocatalytic efficiency.

## EXPERIMENTAL

All chemical precursors employed in the sonochemical synthesis of metal oxide nanostructures were of analytical (AR) grade purity and procured from SDFCL Chemistry Ltd. The metallic precursor utilised was zinc acetate dihydrate [$Zn(CH_3COO)_2{\cdot}2H_2O$, m.w. = 219.51 g $mol^{-1}$). Ultra-pure deionised water (resistivity ≥ 18.2 MΩ·cm) functioned as the reaction medium and solvent system. The solution pH was adjusted to 9.0 ± 0.2 through dropwise addition of standardised 0.1 M NaOH solution. All chemical reagents were used without additional purification procedures.

**Ultrasonic-assisted sonochemical synthesis of ZnO NPs:** The sonochemical method was employed using zinc acetate dihydrate as precursor. In brief, a stoichiometric aqueous solution was prepared by dissolving zinc acetate in deionised water at a molar ratio of 1:3 ($Zn^{2+}$:$OH^-$). The mixture was homogenised *via* magnetic stirring for 15 min. Subsequently, 0.1 M NaOH was added dropwise to adjust the pH to 9.0 ± 0.2, initiating hydrolysis and forming $Zn(OH)_2$ intermediates. The reaction mixture was subjected to ultrasonic irradiation (20-40 kHz frequency, 750 W power, 50% amplitude) for 60 min at 25 ± 2 ºC using a titanium probe homogenizer.

**Characterisation:** Thermogravimetric analysis (TGA) using a TGA55 with TRIOS software was performed on ~10 mg samples from 35 ºC to 700 ºC under nitrogen at 20 ºC/min. X-ray diffraction (XRD) was conducted on a Rigaku Miniflex 600 (Cu*K*α, λ = 1.5406 Å) in the 2θ range of 20º-80º at 2º/min. FESEM analysis (JEOL JSM-7600F) provided SEI resolution of 1.0 nm at 15 kV and 1.5 nm at 1 kV, with magnification up to 1,000,000×. HRTEM was performed using an FEI Tecnai G2 F30 (point resolution: 2.0 Å; 300 kV). UV–Vis spectroscopy was carried out using a UV-1800 Series spectrophotometer (200-1100 nm). FTIR analysis was measured using a Shimadzu spectrometer. Oxidation of ZnO nanoparticles under 366 nm UV light was studied using a 10 ppm dye solution, with absorbance measured at 665 nm.

## RESULTS AND DISCUSSION

**Thermal studies:** The thermogravimetric analysis (TGA) curve of ZnO NPs in Fig. 1 reveals a two-step weight loss profile between 35 ºC and 700 ºC under a $N_2$ atmosphere. The initial minor weight loss (~0.5%) below 150 ºC is attributed to the evaporation of physically adsorbed moisture and volatile surface contaminants. A more pronounced weight loss occurs between 200 ºC and 400 ºC, corresponding to the decomposition of residual organic compounds or unreacted precursors from the synthesis process. Beyond 400 ºC, the curve stabilizes, indicating thermal stability of the ZnO phase. The derivative thermogravimetric (DTG) curve shows a sharp peak near 80 ºC and a broader minimum around 300 ºC, confirming the stepwise decomposition behaviour. The total weight loss is minimal (~3.5%), demonstrating that the ZnO NPs exhibit excellent thermal stability, suitable for high-temperature applications. The observed thermal transitions affirm the high purity and crystalline nature of the ZnO NPs synthesised [27,28].

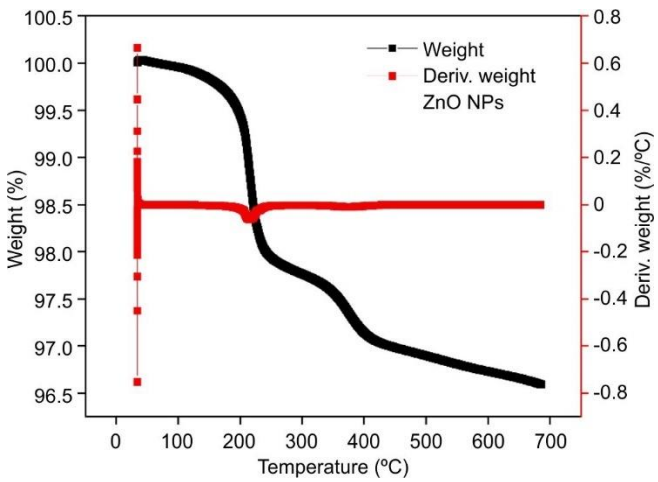


Fig. 1. Thermogravimetric analysis of prepared ZnO NPs

**XRD studies:** The crystalline structure and phase composition of the sonochemically synthesised ZnO NPs exhibiting wurtzite-type hexagonal crystal structure were characterised

using powder X-ray diffraction (PXRD) analysis. The X-ray diffraction (XRD) pattern of ZnO NPs confirms the formation of a highly crystalline structure (Fig. 2). The diffraction peaks observed at 2θ values of approximately 31.7º, 34.4º, 36.2º, 47.5º, 56.6º, 62.8º, 66.3º, 67.9º, 69.1º, 72.6º and 76.9º correspond to the (100), (002), (101), (102), (110), (103), (200), (112), (201) and (202) planes, respectively [29]. These reflections match well with the standard data (JCPDS card No. 36-1451) for the hexagonal wurtzite structure of ZnO indicating phase purity without any secondary phases or impurities [30].

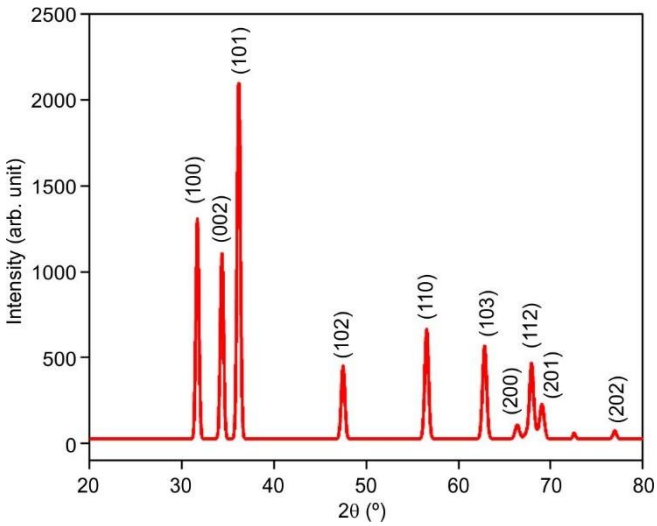


Fig. 2. X-ray diffraction pattern of prepared ZnO NPs

The most intense peak at (101) reflects the preferential orientation of ZnO NPs crystallites along this plane, which is commonly reported in wurtzite ZnO due to its thermodynamic stability. The sharp and narrow peaks denote well-defined crystallinity and nanoscale grain size. The absence of extraneous peaks further supports the high phase purity of the synthesised ZnO NPs. The wurtzite structure of ZnO belongs to the hexagonal crystal system with space group $P6_3mc$. This structure was characterised by tetrahedral coordination of $Zn^{2+}$ and $O^{2-}$ ions, which contributes to the anisotropic growth along the *c*-axis. From Table-1, it can be observed that as the 2θ values span from ~31.69º to ~81.40º, correspond to various prominent planes of the hexagonal wurtzite ZnO structure. The interplanar spacing (*d*) decreases systematically with increasing 2θ, ranging from 2.82 Å for the (100) plane to 1.18 Å for the high-index (104) plane. This trend confirms the inverse relationship between *d*-spacing and diffraction angle.

The 1/d values show a consistent increase, indicative of higher crystallographic plane densities at higher angles. Using eqn. 4, the lattice constant 'a' of the prepared ZnO NPs was determined [31]:

$$d_{hkl} = \frac{a}{(h^2 + k^2 + l^2)^{1/2}} \quad (4)$$

where (*h k l*) are the planes and d is the interplanar distance. The parameter a/d and derived values of lattice constant a show minor variation around an average of ~3.517 Å, consistent with the standard a-parameter of hexagonal ZnO, validating the structural integrity prepared ZnO NPs. The values of $\sqrt{(h^2 + k^2 + l^2)}$ assist in assessing the geometric contribution of each plane to the diffraction pattern, aligning well with the theoretical values. The calculated values of 2sin θ and sin θ demonstrate increasing diffraction vector magnitudes for higher-index planes, suggesting improved crystallinity and well-ordered lattice planes. No significant deviation from expected hexagonal symmetry was observed, indicating the high purity and phase stability of the synthesised ZnO NPs. The crystallite size can be further estimated using the Debye-Scherrer formula (eqn. 5) based on the FWHM of the most intense peak. This equation indicates that for crystallites smaller than a nanometer, the coherently scattering domains are even smaller than the crystallites themselves [32]:

$$D = \frac{K\lambda}{\beta \cos\theta} \quad (5)$$

where K is the dimensionless form factor, λ is the wavelength (1.5406 Å); β is the FWHM and θ is the angle.

According to Table-2, the crystallite size determined using the two techniques exhibits good agreement. The XRD data reveals ZnO nanoparticles with an average crystallite size of approximately 21.6 nm, calculated using Debye-Scherrer's formula. Significant size variation is observed across different crystallographic planes (ranging from 17.6 nm to 31.0 nm), indicating anisotropic growth.

Another parameter, dislocation density (δ), a measure of crystal defects, inversely correlates with size, reaching its highest value ($3.23 \times 10^{-3}$ nm$^{-2}$) for the smallest crystallites. The lattice strain was determined by eqn. 6 [33]:

TABLE-1
CRYSTALLOGRAPHIC PARAMETERS OF ZnO NANOPARTICLES CALCULATED FROM XRD DATA

| Miller indices | | | Diffraction angles | | Sine values | | Interplanar spacing | Lattice parameters | | | | |
|---|---|---|---|---|---|---|---|---|---|---|---|---|
| *h* | *k* | *l* | 2θ | θ | Sin θ | 2Sin θ | d | a | $(a/d)^2$ | $(h^2 + k^2 + l^2)$ | SQRT | 1/d |
| 1 | 0 | 0 | 31.69 | 15.84 | 0.273 | 0.546 | 2.82 | 2.820 | 8.831 | 1.00 | 1.000 | 0.355 |
| 1 | 0 | 1 | 36.183 | 18.09 | 0.311 | 0.621 | 2.48 | 3.507 | 11.419 | 2.00 | 1.414 | 0.403 |
| 1 | 0 | 2 | 47.49 | 23.74 | 0.403 | 0.805 | 1.91 | 4.276 | 19.202 | 5.00 | 2.236 | 0.523 |
| 1 | 1 | 0 | 56.56 | 28.28 | 0.474 | 0.948 | 1.62 | 2.299 | 26.579 | 2.00 | 1.414 | 0.615 |
| 1 | 0 | 3 | 62.80 | 31.42 | 0.521 | 1.043 | 1.47 | 4.672 | 32.178 | 10.0 | 3.162 | 0.677 |
| 1 | 1 | 2 | 67.93 | 33.96 | 0.559 | 1.118 | 1.37 | 3.376 | 36.965 | 6.00 | 2.449 | 0.726 |
| 2 | 0 | 0 | 66.37 | 33.19 | 0.547 | 1.095 | 1.40 | 2.814 | 35.482 | 4.00 | 2.000 | 0.711 |
| 2 | 0 | 1 | 69.07 | 34.53 | 0.567 | 1.134 | 1.35 | 3.037 | 38.058 | 5.00 | 2.236 | 0.736 |
| 2 | 0 | 2 | 76.95 | 38.47 | 0.622 | 1.245 | 1.23 | 3.501 | 45.843 | 8.00 | 2.828 | 0.808 |
| 1 | 0 | 4 | 81.40 | 40.70 | 0.652 | 1.304 | 1.18 | 4.869 | 50.358 | 17.0 | 4.123 | 0.847 |

TABLE-2
X-RAY DIFFRACTION (XRD) DATA OF ZnO NANOPARTICLES

| 2θ | θ | | FWHM | | Cos θ | Crystallite size (D) | Dislocation density (δ) | Lattice strain (ε) |
|---|---|---|---|---|---|---|---|---|
| | Degree | Radian | Degree | Radians | | nm | $\delta \times 10^3$ (nm$^{-2}$) | $\varepsilon \times 10^{-3}$ |
| 31.70 | 15.85 | 0.28 | 0.39 | 0.007 | 0.96 | 21.31 | 2.20 | 0.48 |
| 36.18 | 18.09 | 0.32 | 0.41 | 0.007 | 0.95 | 20.28 | 2.43 | 0.59 |
| 47.49 | 23.75 | 0.41 | 0.45 | 0.008 | 0.92 | 19.19 | 2.72 | 0.87 |
| 56.56 | 28.28 | 0.49 | 0.48 | 0.008 | 0.88 | 18.93 | 2.79 | 1.12 |
| 62.84 | 31.42 | 0.55 | 0.51 | 0.009 | 0.85 | 18.09 | 3.06 | 1.37 |
| 67.94 | 33.97 | 0.59 | 0.46 | 0.008 | 0.83 | 21.05 | 2.26 | 1.34 |
| 66.38 | 33.19 | 0.58 | 0.54 | 0.009 | 0.84 | 17.59 | 3.23 | 1.54 |
| 69.07 | 34.54 | 0.60 | 0.54 | 0.009 | 0.82 | 17.76 | 3.17 | 1.63 |
| 76.96 | 38.48 | 0.67 | 0.44 | 0.008 | 0.78 | 23.25 | 1.85 | 1.51 |
| 81.41 | 40.70 | 0.71 | 0.34 | 0.006 | 0.76 | 31.04 | 1.04 | 1.27 |
| 34.36 | 17.18 | 0.30 | 0.40 | 0.007 | 0.96 | 20.67 | 2.34 | 0.54 |
| 72.56 | 36.28 | 0.63 | 0.33 | 0.006 | 0.81 | 30.30 | 1.09 | 1.04 |

$$\varepsilon = \frac{\beta s}{4 \tan \theta} \quad (6)$$

here, βs represents the full width at half maximum (FWHM), which indicates the broadening of the peak and θ is the angle. Lattice strain (ε) generally increases with diffraction angle (2θ), varying from $0.48 \times 10^{-3}$ to $1.63 \times 10^{-3}$. This trend suggests cumulative lattice distortions at higher angles. The broadening of peaks (FWHM) also increases with 2θ, contributing to the observed size variation. Data inconsistencies, notably in FWHM (rad) calculations for some peaks (67.94º and 76.96º), require verification, but the overall results confirm nanocrystalline ZnO with moderate strain and defect density.

**EDS analysis:** The energy-dispersive X-ray spectroscopy (EDS) spectrum in Fig. 3 confirms the elemental composition of the synthesised nanoparticles. Predominant peaks for zinc (Zn) and oxygen (O) validate the formation of ZnO, with near-stoichiometric atomic ratios (~1:1) indicating phase purity. Minor carbon (C) signals observed at ~0.28 keV are attributed to incidental hydrocarbon adsorption from ambient exposure, which is consistent with the presence of surface-bound organic species identified by FTIR analysis. The absence of other elemental peaks confirms the absence of significant synthetic impurities or dopants, which aligns with the XRD and UV-Vis data, collectively confirming high-purity ZnO NPs suitable for functional applications where compositional integrity is critical.

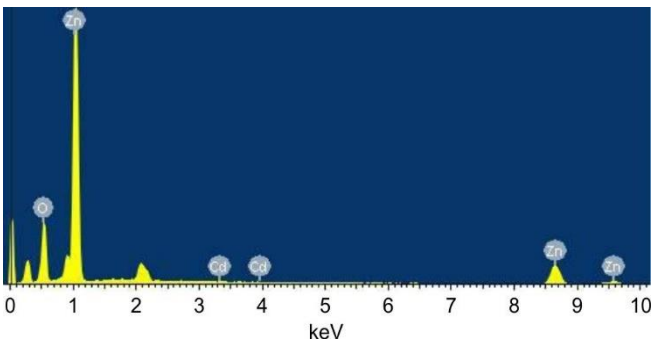


Fig. 3. EDS spectrum of ZnO NPs

**Morphological studies:** FE-SEM images (Fig. 4a-c) at 50,000× magnification reveal quasi-spherical ZnO NPs with moderate dispersibility, though some agglomeration is observed due to high surface energy and interparticle interactions, whereas the particle size histogram (Fig. 4d) demonstrates a unimodal size distribution ranging from 35-70 nm. The calculated mean diameter was found to be 48.22 nm, which is significantly larger than the XRD-derived crystallite size (21.6 nm). This discrepancy confirms polycrystalline particle architecture, where each nanoparticle comprises multiple smaller crystallites (domains) separated by intra-particle grain boundaries. The distribution exhibits slight positive skewness, indicating a minor population of larger aggregates likely formed through Ostwald ripening during synthesis [34,35]. These morphological characteristics directly influence the functional properties: nanoscale dimensions enhance surface-to-volume ratios for catalytic applications, while crystallite boundaries within particles may facilitate charge carrier separation in optoelectronic devices.

**HR-TEM studies:** The high-resolution TEM images (Fig. 5a-e) confirm the single-crystalline nature of ZnO NPs, revealing well-defined lattice fringes with measured interplanar spacings of ~0.28 nm and ~0.26 nm. These correspond to the (100) and (002) planes of hexagonal wurtzite structure, aligning with XRD results. The SAED patterns (Fig. 5f) exhibit sharp concentric rings indexed to (100), (002) and (101) planes, confirming crystallographic orientation [36]. The minimal lattice defects and uniform fringe continuity indicate high crystallinity, while observed particle sizes (~20-25 nm) correlate with the Debye-Scherrer calculations.

**FTIR studies:** The FTIR spectrum (Fig. 6) reveals the characteristic vibrational modes and surface functionalities of the synthesised ZnO NPs. A broad, intense absorption band centered at 3446 cm$^{-1}$ is attributed to O–H stretching vibrations, indicating the presence of surface-adsorbed water molecules or hydroxyl groups, a common feature in hydrophilic nanomaterials. The distinct peak at 2927 cm$^{-1}$ corresponds to asymmetric C–H stretching vibrations, suggesting potential residual organic moieties from precursors or surfactants used during synthesis. The peaks observed at 1549 and 1428 cm$^{-1}$ are indicative of asymmetric and symmetric stretching modes of carboxylate groups ($COO^-$), respectively, possibly arising from surface capping agents or atmospheric carbon dioxide adsorption. The band at 1096 cm$^{-1}$ may be assigned to C–O stret-

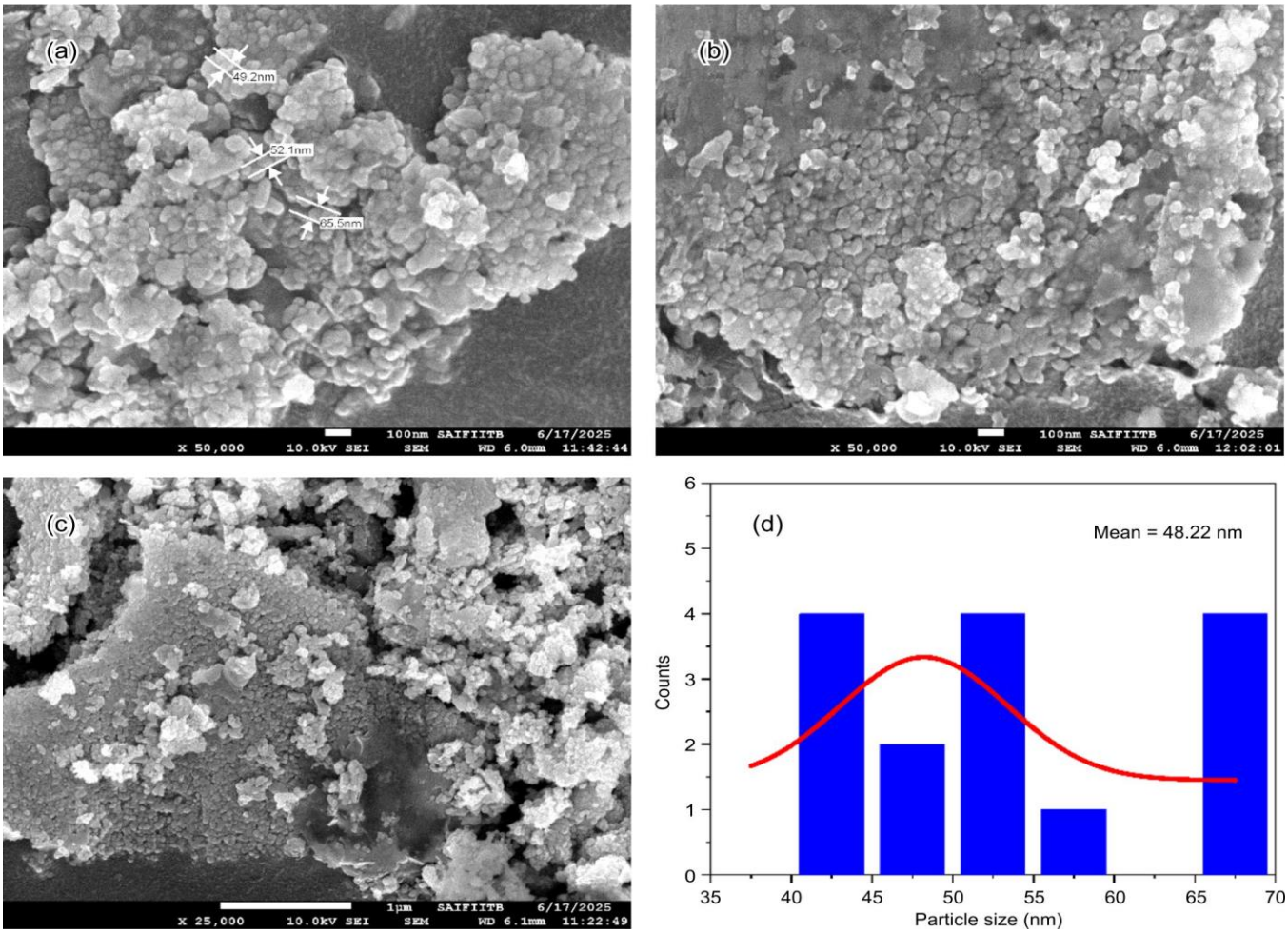


Fig. 4. (a-c) SEM micrograph of ZnO NPs at 50,000× magnification and (d) particle size distribution histogram derived from SEM analysis

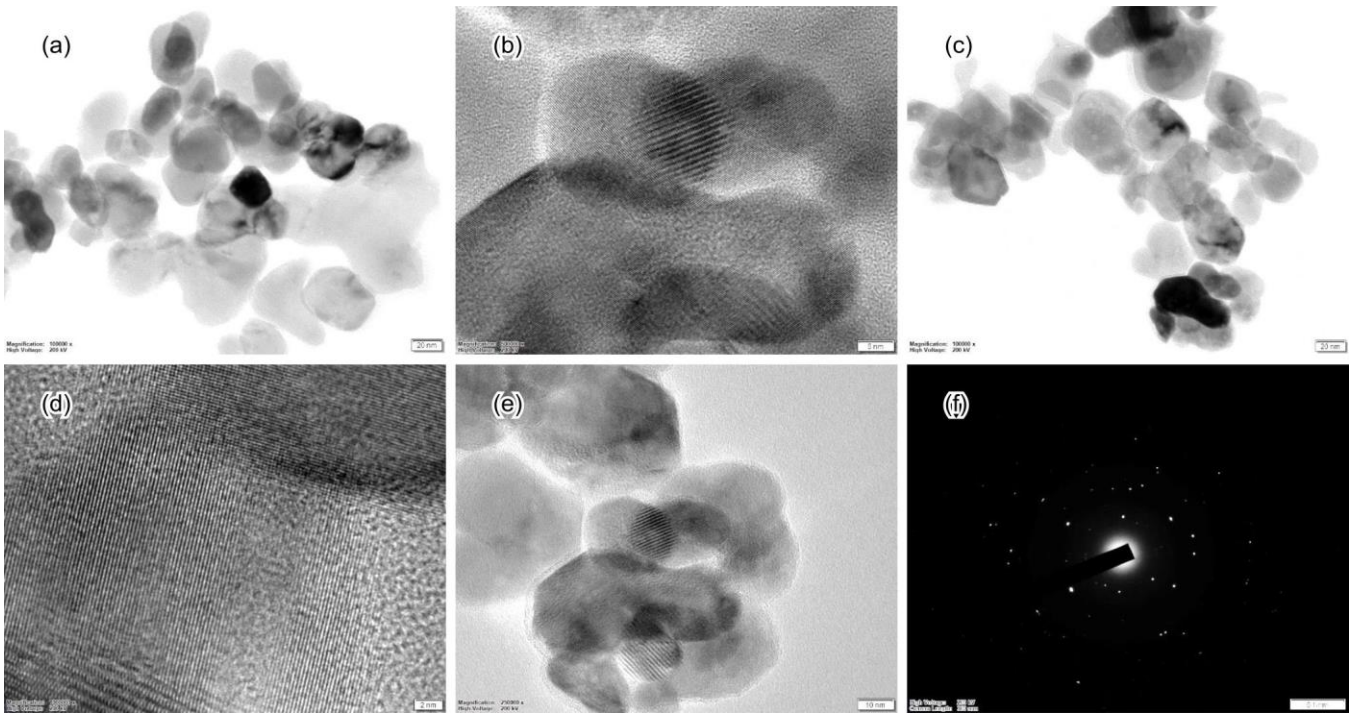


Fig. 5. (a-e) HR-TEM micrographs of ZnO NPs and (f) SAED pattern derived from TEM

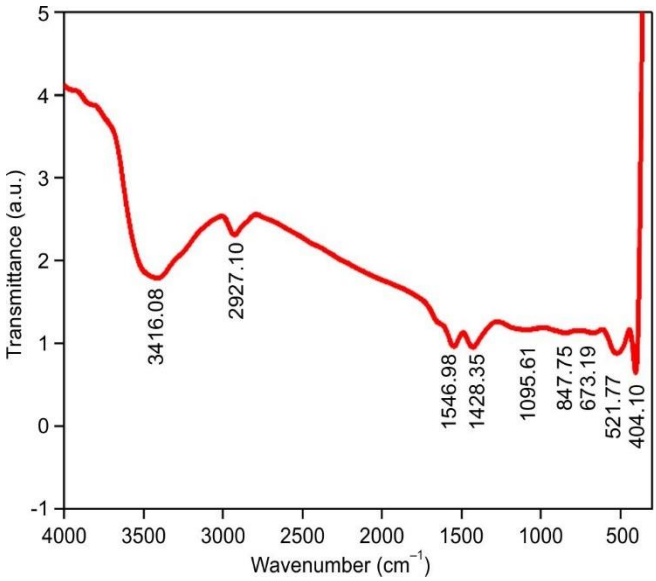


Fig. 6. FTIR spectrum of synthesised ZnO NPs

ching vibrations [37]. Significantly, the fingerprint region below 1000 cm$^{-1}$ confirms the ZnO lattice, the prominent absorption at 848 cm$^{-1}$ corresponds to Zn–O stretching modes, while the peaks at 673 and 404 cm$^{-1}$ are characteristic of metal-oxygen (Zn–O) vibrational modes within the wurtzite crystal structure [38,39]. These low-frequency bands provide definitive evidence of ZnO NPs formation, with slight shifts arising from nanoscale effects such as surface phonon modes and quantum confinement. The spectrum confirms successful ZnO NPs synthesis while indicating surface hydroxylation and residual organics that may influence interfacial properties.

**UV-Vis studies:** The UV-Vis absorption spectrum (Fig. 7) exhibits a distinct, sharp absorption edge around ~370-380 nm, characteristic of the bandgap transition in ZnO NPs. This represents a blue-shift relative to bulk ZnO (~387 nm), confirming quantum confinement effects due to nanoscale dimensions. Fig. 8 presents the band gap energy ($E_g$), determined using Tauc's plot and the Kubelka-Munk equation (eqn. 7) [40]:

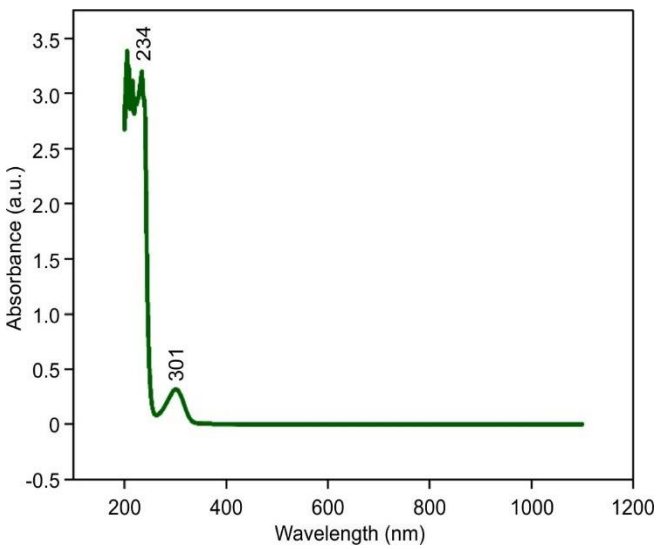


Fig. 7. UV-Vis absorption spectrum of colloidal ZnO nanoparticles

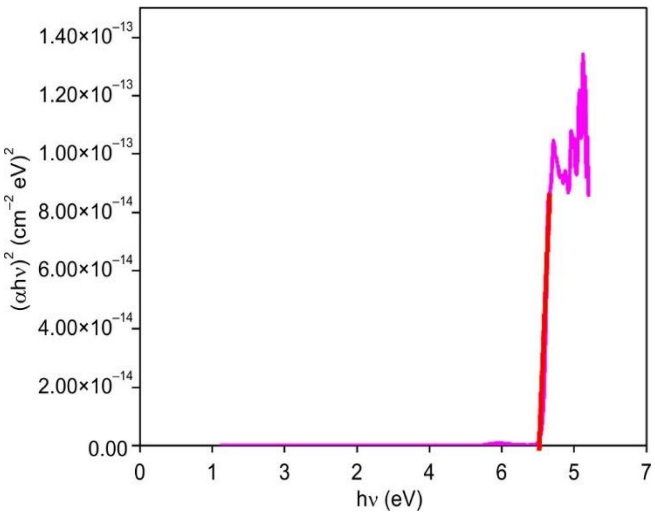


Fig. 8. Tauc plot for direct bandgap determination of ZnO NPs

$$(\alpha h\nu)^n = K(h\nu - E_g) \quad (7)$$

where hν represents the photon energy; $E_g$ is the band gap energy; K is an energy-dependent constant and n varies based on the type of transition. Specifically, η equals 2 and 1/2 for allowed direct and indirect transitions, respectively and α denotes the absorption coefficient, which is derived from the Beer-Lambert's law (eqn. 8) [41,42]:

$$\alpha = \frac{2.303 \times A}{t} \quad (8)$$

where α represents the absorbance; and t is the cuvette's thickness (1 cm) [43]. The direct bandgap of ZnO NPs was found to be ~3.27 eV. This widening from bulk $E_g$ of ZnO (3.37 eV) arises from spatial confinement of charge carriers, consistent with XRD-determined crystallite sizes (~21 nm).

The steep absorption edge indicates monodisperse particle distribution and high crystallinity, while the absence of secondary peaks suggests phase purity. The weak absorption tail beyond 400 nm may arise from light scattering by nanoparticles or minor sub-bandgap defects. The observed blue-shift and enlarged bandgap [44] directly correlate with the size-dependent optoelectronic properties of prepared ZnO NPs, making this material suitable for UV-photodetectors, photocatalytic applications and optoelectronic devices where tunable band alignment is essential.

**Photocatalytic degradation of methylene blue dye (MB) with ZnO NPs:** The photocatalytic degradation of methylene blue dye was investigated under ultraviolet (UV) irradiation at a wavelength of 366 nm using ZnO NPs as a photocatalyst (Fig. 9a). The initial dye concentration was maintained at 10 ppm and degradation was monitored *via* UV-Vis spectroscopy at the maximum absorption wavelength of 665 nm. ZnO, a wide bandgap semiconductor (~3.37 eV), exhibits strong photocatalytic activity under UV light due to the generation of electron-hole pairs. These photo-induced charge carriers participate in redox reactions, producing reactive oxygen species (ROS), particularly hydroxyl radicals (OH) and superoxide anions ($O_2^-$), which oxidize and decompose the dye molecules. The degradation curves reveal a pronounced decline in absorbance intensity over time for the MB + ZnO system, in

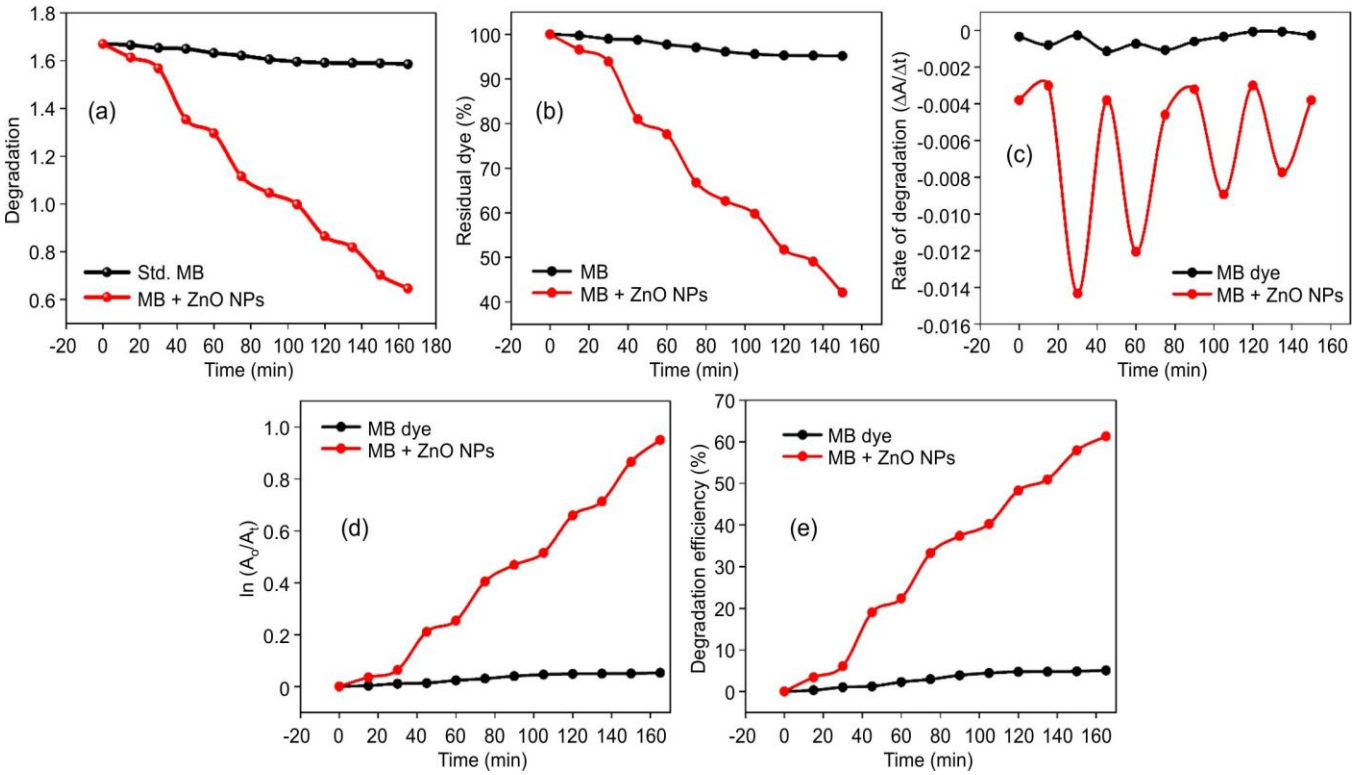


Fig. 9. Photocatalytic degradation results of methylene blue (MB) dye under UV irradiation (λ = 366 nm) using ZnO NPs as a catalyst. The graphs compare (a) degradation of MB dye, (b) residual dye percentage, (c) rate of degradation (ΔA/Δt), (d) pseudo-first-order kinetic plot $\ln(A_o/A_t)$ *vs.* time and (e) degradation efficiency (%) for MB dye with and without ZnO NPs

contrast to the nearly constant profile observed for MB alone, indicating minimal self-degradation [45]. The percentage degradation (D%) can be calculated by using rel. (eqn. 9):

$$D\ (\%) = \left(\frac{C - C_t}{C}\right) \times 100 \qquad (9)$$

where C and $C_t$ are the initial and final dye concentration at time t, respectively.

The residual dye percentage decreased significantly with irradiation time in the ZnO NPs system, dropping below 50% after 160 min as shown in Fig. 9b. The degradation efficiency reached approximately 60%, demonstrating the effective photocatalytic potential of ZnO [46]. Moreover, the rate of degradation (ΔA/Δt) exhibited periodic fluctuations, likely due to dynamic surface interactions and intermediate formation during photodegradation as shown in Fig. 9c. The kinetic plot, based on the pseudo-first-order model ($\ln(A_o/A_t)$ *vs.* time) as seen in Fig. 9d, showed a linear relationship for the ZnO NPs added system, confirming first-order kinetics. This behaviour emphasizes the role of ZnO NPs in accelerating dye oxidation through enhanced ROS production [47]. Overall, ZnO NPs act as an efficient photocatalyst for the oxidative degradation of MB dye under UV light, making them suitable for advanced oxidation processes in wastewater treatment as shown in Fig. 9e.

## Conclusion

The ultrasonic assisted sonochemical synthesis of phase-pure, crystalline ZnO NPs is successfully conducted and characterised. Thermal results support the surface organics with a 3.5% mass loss (200-400 ºC), beyond which ZnO NPs demonstrates thermal stability. XRD analysis validates the hexagonal wurtzite structure (space group $P6_3mc$), exhibiting lattice parameter a ≈ 3.517 Å and an average crystallite size of 21.6 nm. EDS confirms the stoichiometric Zn:O composition with trace carbon impurities. Morphologically, SEM/TEM reveal quasi-spherical nanoparticles with mean size 48.22 nm for such a with single-crystalline domains, evidenced by lattice fringes corresponding to (100) and (002) planes (0.28/0.26 nm *d*-spacing). The size disparity between XRD crystallites and SEM particles indicates polycrystalline aggregates. FTIR identifies residual organic moieties (C–H at 2927 $cm^{-1}$, carboxylates at 1549-1428 $cm^{-1}$) and definitive Zn–O lattice vibrations (848-404 $cm^{-1}$). Optical studies reveal a quantum-confined bandgap of 3.27 eV (blue-shifted from bulk) *via* UV-Vis and Tauc plot analysis. ZnO NPs exhibit exceptional photocatalytic efficiency under UV irradiation (366 nm), degrading methylene blue dye (10 ppm) *via* pseudo-first-order kinetics with >50% removal in 160 min. This multifunctional performance stemming from optimal crystallinity, wide bandgap and surface reactivity positions these nanoparticles as robust candidates for advanced oxidation processes in environmental remediation and UV-photocatalysis.

## ACKNOWLEDGEMENTS

The authors gratefully acknowledge the Sophisticated Analytical Instrument Facility (SAIF), Indian Institute of Technology Bombay, Mumbai (IITB) for providing SEM, EDS and HRTEM analysis support for this research work.

## CONFLICT OF INTEREST

The authors declare that there is no conflict of interests regarding the publication of this article.

## DECLARATION OF AI-ASSISTED TECHNOLOGIES

During the preparation of this manuscript, the authors used an AI-assisted tool(s) to improve the language. The authors reviewed and edited the content and take full responsibility for the published work.

## REFERENCES


1. S. Chatterjee, P. Bhanja, D. Ghosh, P. Kumar, S. Kanti Das, S. Dalapati and A. Bhaumik, *ChemSusChem*, **14**, 408 (2021); https://doi.org/10.1002/cssc.202002136
2. M. Xue, F. Li, W. Peng, Q. Zhu and Y. He, *Nanoenergy Adv.*, **3**, 401 (2023); https://doi.org/10.3390/nanoenergyadv3040020
3. M. Montero-Muñoz, J.E. Ramos-Ibarra, J.E. Rodríguez-Páez, M.D. Teodoro, G.E. Marques, A.R. Sanabria, P.C. Cajas, C.A. Páez, B. Heinrichs and J.A.H. Coaquira, *Appl. Surf. Sci.*, **448**, 646 (2018); https://doi.org/10.1016/j.apsusc.2018.04.105
4. J. Wang, R. Chen, L. Xiang and S. Komarneni, *Ceram. Int.*, **44**, 7357 (2018); https://doi.org/10.1016/j.ceramint.2018.02.013
5. B. Li, L. Ren, D. Jiang, M. Jia, M. Zhang, G. Xu, Y. Sun, L. Hou, C. Yuan and Y. Yuan, *Next Energy*, **7**, 100222 (2025); https://doi.org/10.1016/j.nxener.2024.100222
6. S.A. Sobha, J. Johnson and K.P. Abhina, *J. Alloys Compd.*, **1037**, 182365 (2025); https://doi.org/10.1016/j.jallcom.2025.182365
7. A. Alsalme, K.M. Elmoneim, N.N. Mohammed, K. Mohamed, M. Abdel-Messih, A. Sultan and M. Ahmed, *Ceram. Int.*, **50**, 50622 (2024); https://doi.org/10.1016/j.ceramint.2024.09.407
8. Z. Li, J. Dong, H. Zhang, Y. Zhang, H. Wang, X. Cui and Z. Wang, *Nanoscale Adv.*, **3**, 41 (2021); https://doi.org/10.1039/D0NA00753F
9. S. Shenoy, S. Ahmed, I.M. Lo, S. Singh and K. Sridharan, *Mater. Res. Bull.*, **140**, 111290 (2021); https://doi.org/10.1016/j.materresbull.2021.111290
10. S. Thakur and S.K. Mandal, *Mater. Adv.*, **2**, 511 (2021); https://doi.org/10.1039/D0MA00781A
11. A. Serrano-Lázaro, K. Portillo-Cortez, M. B. de la Mora Mojica and J. C. Durán-Álvarez, *Nanomaterials*, **15**, 1627 (2025); https://doi.org/10.3390/nano15211627
12. S.J. Armaković, S. Armaković, A. Bilić and M.M. Savanović, *Catalysts*, **15**, 793 (2025); https://doi.org/10.3390/catal15080793
13. L.-C. Cheng, S. Brahma, J.-L. Huang and C.-P. Liu, *Mater. Sci. Semicond. Process.*, **146**, 106703 (2022); https://doi.org/10.1016/j.mssp.2022.106703.
14. W. Ouyang, J. Chen, Z. Shi and X. Fang, *Appl. Phys. Rev.*, **8**, 031315 (2021); https://doi.org/10.1063/5.0058482
15. M.N. Rezaie, S. Mohammadnejad and S. Ahadzadeh, *Opt. Laser Technol.*, **138**, 106896 (2021); https://doi.org/10.1016/j.optlastec.2020.106896
16. B. Barman, S.K. Swami and V. Dutta, *Mater. Sci. Semicond. Process.*, **129**, 105801 (2021); https://doi.org/10.1016/j.mssp.2021.105801
17. J. Rodrigues, S.O. Pereira, J. Zanoni, C. Rodrigues, M. Brás, F.M. Costa and T. Monteiro, *Chemosensors*, **10**, 39 (2022); https://doi.org/10.3390/chemosensors10020039
18. W. Wanas, S.A. Abd El-Kareem, S. Ebrahim, M. Soliman and M. Karim, *Sci. Rep.*, **13**, 27 (2023); https://doi.org/10.1038/s41598-022-27111-z
19. R. Sha, A. Basak, P.C. Maity and S. Badhulika, *Sens. Actuators Rep.*, **4**, 100098 (2022); https://doi.org/10.1016/j.snr.2022.100098
20. R.K. Pandey, J. Dutta, S. Brahma, B. Rao and C.-P. Liu, *J. Phys Mater.*, **4**, 044011 (2021); https://doi.org/10.1088/2515-7639/ac130a
21. C. Sun, J. Zhang, Y. Zhang, F. Zhao, J. Xie, Z. Liu, J. Zhuang, N. Zhang, W. Ren and Z.-G. Ye, *Appl. Surf. Sci.*, **562**, 150126 (2021); https://doi.org/10.1016/j.apsusc.2021.150126
22. P. Mosallanezhad, H. Nazockdast, Z. Ahmadi and A. Rostami, *Front. Bioeng. Biotechnol.*, **10**, 1027351 (2022); https://doi.org/10.3389/fbioe.2022.1027351
23. K.G. Krishna, G. Umadevi, S. Parne and N. Pothukanuri, *J. Mater. Chem. C Mater. Opt. Electron. Devices*, **11**, 3906 (2023); https://doi.org/10.1039/D2TC04690C
24. S. Mondal and B. Bhattacharjee, *The Scientific Temper*, **15**, 2460 (2024); https://doi.org/10.58414/SCIENTIFICTEMPER.2024.15.3.01
25. Z. Wang, M.R. Bockstaller and K. Matyjaszewski, *ACS Mater. Lett.*, **3**, 599 (2021); https://doi.org/10.1021/acsmaterialslett.1c00145
26. S.S. Low, M. Yew, C.N. Lim, W.S. Chai, L.E. Low, S. Manickam, B.T. Tey and P.L. Show, *Ultrason. Sonochem.*, **82**, 105887 (2022); https://doi.org/10.1016/j.ultsonch.2021.105887
27. J. Rami, C. Patel, C. Patel and M. Patel, *Mater. Today Proc.*, **43**, 655 (2021); https://doi.org/10.1016/j.matpr.2020.12.554
28. I.A. Channa, J. Ashfaq, S.J. Gilani, A.A. Shah, A.D. Chandio and M.N.B. Jumah, *Coatings*, **12**, 897 (2022); https://doi.org/10.3390/coatings12070897
29. T.T. Dao, T.L.N. Vo, A.T. Duong, D.L. Nguyen, V.S. Luong and H.T. Nguyen, *J. Sol-Gel Sci. Technol.*, **115**, 1391 (2025); https://doi.org/10.1007/s10971-025-06828-z
30. T. Asaulyuk, Y. Saribyekova, O. Semeshko and I. Kulish, *Herald Khmelnytskyi Natl. Univ. Tech. Sci.*, **311**, 35 (2022); https://doi.org/10.31891/2307-5732-2022-311-4-35-41
31. Y. Sakamoto, T.W. Kim, R. Ryoo and O. Terasaki, *Angew. Chem. Int. Ed.*, **43**, 5231 (2004); https://doi.org/10.1002/anie.200460449
32. A. Shrivastava and A. Shrivastava, *AIP Conf. Proc.*, **2352**, 020024 (2021); https://doi.org/10.1063/5.0052721
33. H. Shashidharagowda and S.N. Mathad, *Mater. Sci. Energy Technol.*, **3**, 201 (2020); https://doi.org/10.1016/j.mset.2019.10.008
34. A. Spoială, C.-I. Ilie, R.-D. Trușcă, O.-C. Oprea, V.-A. Surdu, B.Ș. Vasile, A. Ficai, D. Ficai, E. Andronescu and L.-M. Dițu, *Materials*, **14**, 4747 (2021); https://doi.org/10.3390/ma14164747
35. A.C. Mohan and B. Renjanadevi, *Procedia Technol.*, **24**, 761 (2016); https://doi.org/10.1016/j.protcy.2016.05.078
36. Y. Zhu and Y. Zhou, *Appl. Phys., A Mater. Sci. Process.*, **92**, 275 (2008); https://doi.org/10.1007/s00339-008-4533-z
37. A.C. Janaki, E. Sailatha and S. Gunasekaran, *Spectrochim. Acta A Mol. Biomol. Spectrosc.*, **144**, 17 (2015); https://doi.org/10.1016/j.saa.2015.02.041
38. P. Labhane, V. Huse, L. Patle, A. Chaudhari and G. Sonawane, *J. Mater. Sci. Chem. Eng.*, **3**, 39 (2015).
39. T. Thangeeswari, A.T. George and A.A. Kumar, *Indian J. Sci. Technol.*, **9**, 1 (2016); https://doi.org/10.17485/ijst/2016/v9i1/85776
40. S. Elbasuney, G.S. El-Sayyad, H. Tantawy and A.H. Hashem, *RSC Adv.*, **11**, 25961 (2021); https://doi.org/10.1039/D1RA04542C
41. M. Kandasamy, S. Murugesan, M. Selvaraj and M.M. Alam, *Ceram. Int.*, **48**, 6037 (2022); https://doi.org/10.1016/j.ceramint.2021.11.140
42. S.K. Abdel-Aal and A.S. Abdel-Rahman, *J. Electron. Mater.*, **48**, 1686 (2019); https://doi.org/10.1007/s11664-018-06916-7
43. V. Platonov, N. Malinin, R. Vasiliev and M. Rumyantseva, *Chemosensors*, **11**, 227 (2023); https://doi.org/10.3390/chemosensors11040227
44. Z. Song, T.A. Kelf, W.H. Sanchez, M.S. Roberts, J. Rička, M. Frenz and A.V. Zvyagin, *Biomed. Opt. Express*, **2**, 3321 (2011); https://doi.org/10.1364/BOE.2.003321
45. T.-J. Whang, M.-T. Hsieh and H.-H. Chen, *Appl. Surf. Sci.*, **258**, 2796 (2012); https://doi.org/10.1016/j.apsusc.2011.10.134
46. N. Jain, A. Bhargava and J. Panwar, *Chem. Eng. J.*, **243**, 549 (2014); https://doi.org/10.1016/j.cej.2013.11.085
47. J. Lu, I. Batjikh, J. Hurh, Y. Han, H. Ali, R. Mathiyalagan, C. Ling, J.C. Ahn and D.C. Yang, *Optik*, **182**, 980 (2019); https://doi.org/10.1016/j.ijleo.2018.12.016